Synthesis and physical characterization of Ni-doped La$_2$O$_3$ for photocatytic application under sunlight

C. Bilel[1,*] , R. Jbeli[2,*], I. Ben Jemaa[3], Youssef Dabaki[4], Meshal Alzaid[1], F. Saadallah[2], M. Bouaicha[2], and M. Amlouk[5]

[1] *Physics Department, College of Science, Jouf University, P.O. Box 2014, Sakaka, Saudi Arabia*

[2] *Laboratoire de Photovoltaïque, Centre National de Recherches en Sciences des Matériaux, B.P. 95, 2050 Hammam-Lif, Tunisia*

[3] *Laboratoire de Photovoltaıque et Matériaux Semi-Conducteurs, Université de Tunis el Manar, 1002 Tunis, Tunisia*

[4] *Université de Tunis, ENSIT, LR99ES05, 1008 Monfleury, Tunisia*

[5] *Laboratoire de Nanomatériaux Nanotechnologie et Energie (L2NE), Faculté des Sciences de Tunis, Université de Tunis, El Manar, 2092 Tunis, Tunisia*

ABSTRACT

In this paper, Ni was used as a doping element for La$_2$O$_3$ thin films using the spray pyrolysis method. First, the structural properties of obtained films were investigated by means of X-ray diffraction technique and Raman Spectroscopy. Furthermore, the morphological properties were examined by the scanning electron microscopy. Second, the optical properties of these films were examined using the photoluminescence measurements. Moreover, the electrical properties of Ni-doped La$_2$O$_3$ thin films are discussed. Finally, the photocatalytic effects were investigated by controlling the degradation of the both pollutants: methylene blue and methylene orange under sunlight. The La$_2$O$_3$ thin film-doped with Ni could enhance the photocatalysts properties of the film for wastewater treatment under sunlight since a cost-effective chemical process was used to prepare such doped films.

1 Introduction

Lanthanum oxide La$_2$O$_3$ is one of the most attractive oxides semiconductors due to its outstanding and unique chemical and physical properties, such as large band gap (5.5 eV), high relative dielectric constant ($K > 20$), and thermal stability [1]. La$_2$O$_3$ is a potential candidate material for several applications, for example gas sensors [1], biomedicine [2], protective coating layer [3], photocatalysis [4], microelectronics [5], electrodes in solid fuel cells (SOFC) [6], and thermo-electric devices [7]. La$_2$O$_3$ has two typical phases; cubic and hexagonal. Cubic La$_2$O$_3$ (c-La$_2$O$_3$) is stable at low temperature, whereas hexagonal La$_2$O$_3$ (h-La$_2$O$_3$) is more stable at high temperature [8]. Doping lanthanum oxide with a metal is considered an effective way to modify and upgrade such properties like band gap. This binary oxide can be doped with various elements such as: iron [9], silver [10], copper [11], europium [12] and

---

nickel [13]. In particular, ternary oxides based on lanthanum such as $LaFeO_3$, $LaNiO_3$ and $LaCoO_3$ were used in the development of magnetic memory cells and magnetic read heads [14].

Experimentally, La_2O_3 thin layers can be synthesized by several techniques such as ion beam assistant electron-beam evaporation, laser ablation and spray pyrolysis [15–20]. Especially, spray pyrolysis [20] has been widely used for the reason that is a simple method, cheaper cost, and it is ease in controlling experimental inputs for example annealing temperature and carrier gas flow. The control of native oxygen vacancies in oxide layers is carried out by optimizing the concentrations of the precursors and annealing time [21, 22].

Recently, various semiconductor oxides have attracted great attention by many researchers to develop the photocatalysts. In fact, the photocatalysis based on the use of semiconductors is classified as a "Green technology" and it seems to be an appropriate solution for wastewater treatment. In particular, La_2O_3 can be one of the most promising materials in the wastewater treatment applications [23]. La_2O_3 ions doping lead to enhance the adsorption of the organic reactants by forming complexes via their f-orbitals with various organic Lewis bases [24]. From a rapid review in the literature, few attempts have been found regarding the use of La_2O_3 as photocatalyst. For instance, La_2O_3 has been tested as a catalyzer and it has provided great results especially for iron doping [9].

Indeed, this oxide compared to other binary oxides such as ZnO and TiO_2 has a large band gap and the photocatalysis is required under visible radiation. Thus, an appropriate doping could in principle make this oxide working in visible light. For this reason, doping La_2O_3 with Ni may be of interest to photodegrade pollutants in water.

In this work, undoped La_2O_3 and Ni-doped La_2O_3 thin films were obtained using the spray pyrolysis technique. The structural and the morphological properties of these films have been investigated using XRD and the scanning electron microscopy (SEM). The optical properties of samples were investigated using fluorescence spectrometer. The impedance analyzer was used to measure the conductivity of the prepared layers. The photocatalytic effect of layers has been tested by controlling the degradation of the both pollutants methylene blue and methylene orange under sunlight using a spectrophotometer.

2 Experimental

2.1 Preparation of La_2O_3 and Ni-doped La_2O_3 thin films

The preparation of pure La_2O_3 and Ni-doped La_2O_3 samples were carried out according to the following steps. An aqueous solution of [$LaCl_3$, $7H_2O$] with a concentration of 0.02 M is used as a starting precursor to elaborate pure Lanthanum oxide on glass at 460 °C. The nickel-doped Lanthanum oxide films were obtained by adding nickel chloride heptahydrate ($NiCl_3$, $7H_2O$) to the precursor solution, with a doping percentage of 0–5%. At the outset, for homogeinizing the starting solution was stirred at room temperature for 30 min.

The optimization of experimental conditions provides well results in samples preparation. In fact, the distance between the nozzle and the substrate plane was optimized to the optimum value of 27 cm and the substrate temperature was controlled via a thermocouple. Nitrogen was used as gas carrier (0.35 bar) through 0.5 mm diameter nozzle and the volume sprayed is 50 ml. The rate of spray is about 4 ml min^{-1}.

2.2 Technical characterizations

First, both X-ray diffraction and Raman spectroscopy were used to study the structure of pure La_2O_3 and Ni-doped La_2O_3. X-Ray diffraction analysis provided by X'Pert PRO PANalytical difractometer was operated with Cu Kα radiation ($\lambda = 1.5406$ Å) with 2θ ranging from 10° to 80°. Raman Spectra were recorded through a Jobin Yvon HR LabRAM. Ar_+ Laser with wavelength of 488 nm was used as an excitation beam. A scanning electron microscopy SEM (type JOEL-JSM 5400) is used to determinate the morphology of different samples at operating voltage of 10KV. Moreover, the optical properties were studied via Perkin-Elmer LS 55 Fluorescence spectrometer with an excitation radiation of 220 nm. The PL spectra were obtained in the spectral range of 300–900 nm at room temperature. Second, an automatically controlled HP HP4192A analyzer of type Hewlett-Packard HP 4192 is used to determine the electrical properties of the samples: pure La_2O_3, La_2O_3: Ni (1%), La_2O_3: Ni (3%) and La_2O_3: Ni (5%). These measurements were done using tow electrodes at a temperature range between 290 and 370 K and at

a frequency range of 5 Hz–13 MHz. Finally, the photocatalytic experiments were carried out according to the following experimental protocol. The thin films of La_2O_3: Ni of the surface area 2 cm^2 were putted in a beaker in quartz containing 30 mL of 3×10–3 M aqueous methylene blue solution under solar irradiation in June month at a temperature of 36 °C. The solution was placed in the dark for 30 min with stirring to reach the adsorption–desorption equilibrium between the photocatalyst and the dye. In this framework, the follow up of the photocatalytic degradation was performed by means of the measuring of the absorbance of the MB solution by the Schimadzu UV 3100 spectrophotometer in the range of 400–800 nm. The measurements were performed for various periods: 60, 120, 180, 240 and 300 min.

3 Results and discussion

3.1 Structural properties

3.1.1 XRD analysis

The analysis by X-ray diffraction spectroscopy (XRD) of all films shows that the elaborated layers are well structured (Fig. 1a) and characterized by a mixture of two phases. Their preferential orientation is (001) which corresponds to the hexagonal phase. The orientations (001), (100),(400), (134), (440), (622), which are in accordance with JCPDS file no. 83-1345 correspond to the hexagonal phase. The cubic phase is characterized by the orientations (420), (046), (653) which are in accordance with the file (JCPDS:65-3185). For different doping levels, Fig. 1b shows that all peaks shift towards low angles confirming the incorporation of nickel element into the host matrix. In these XRD spectra, there are no peaks related to secondary phases such as $LaNiO_3$ or NiO. This may be due to the low Ni content ([Ni/La] ratio less than 5%).

3.1.2 Scanning electron microscopy (SEM) observations

It is well known that the study of the morphology of thin films provides important insights about their structural and optical properties. Thus, the investigation of the surface morphology (SEM) of the prepared samples is displayed in Fig. 2. The micrographs show that all samples show a flat and
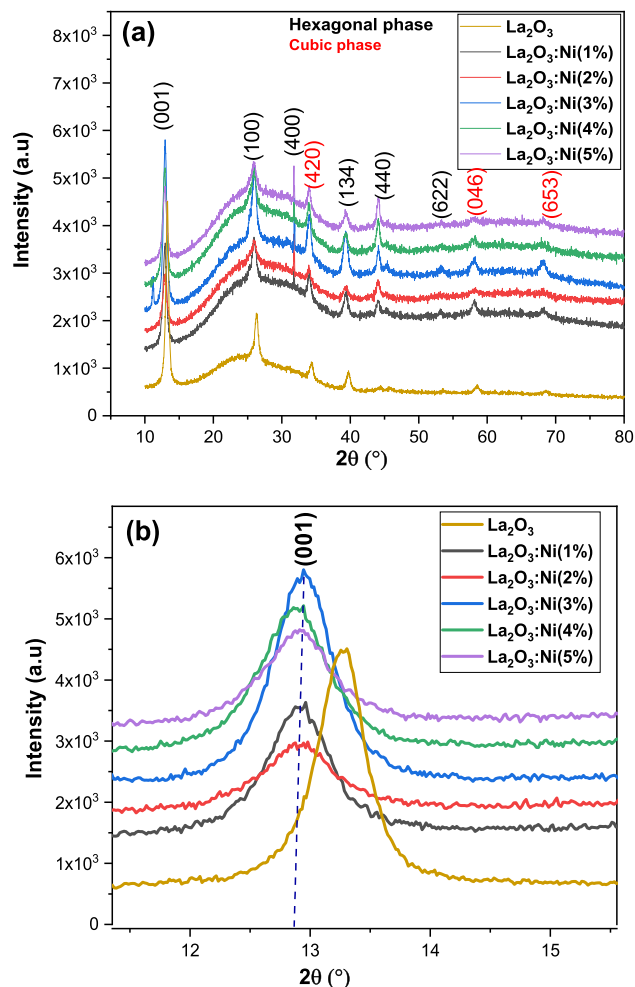

Fig. 1 a X-ray diffractgrams of pure La_2O_3 and Ni doped La_2O_3. b Zoom of the principal orientation (100)

uniform structure surface perturbed by grains with different shapes. In addition, these images display small crystals which are grown separately and coalesced to chains with different lengths. It is important to note that after doping with nickel the size of particles on surface is decreased. Furthermore, the nickel doping leads to better dispersion of the particles and thus improves the surface homogeneity.

3.1.3 Raman study

Raman Spectroscopy technique is recognized to reveal the possible presence of secondary phase. This technique has a high sensitivity to the microstructure and identifies the different defects in the elaborated layers. Figure 3a shows the Raman spectrum of undoped La_2O_3 film. There are four bands located at 125 cm^{-1} 196 cm^{-1}, 337 cm^{-1} and 442 cm^{-1}. The two
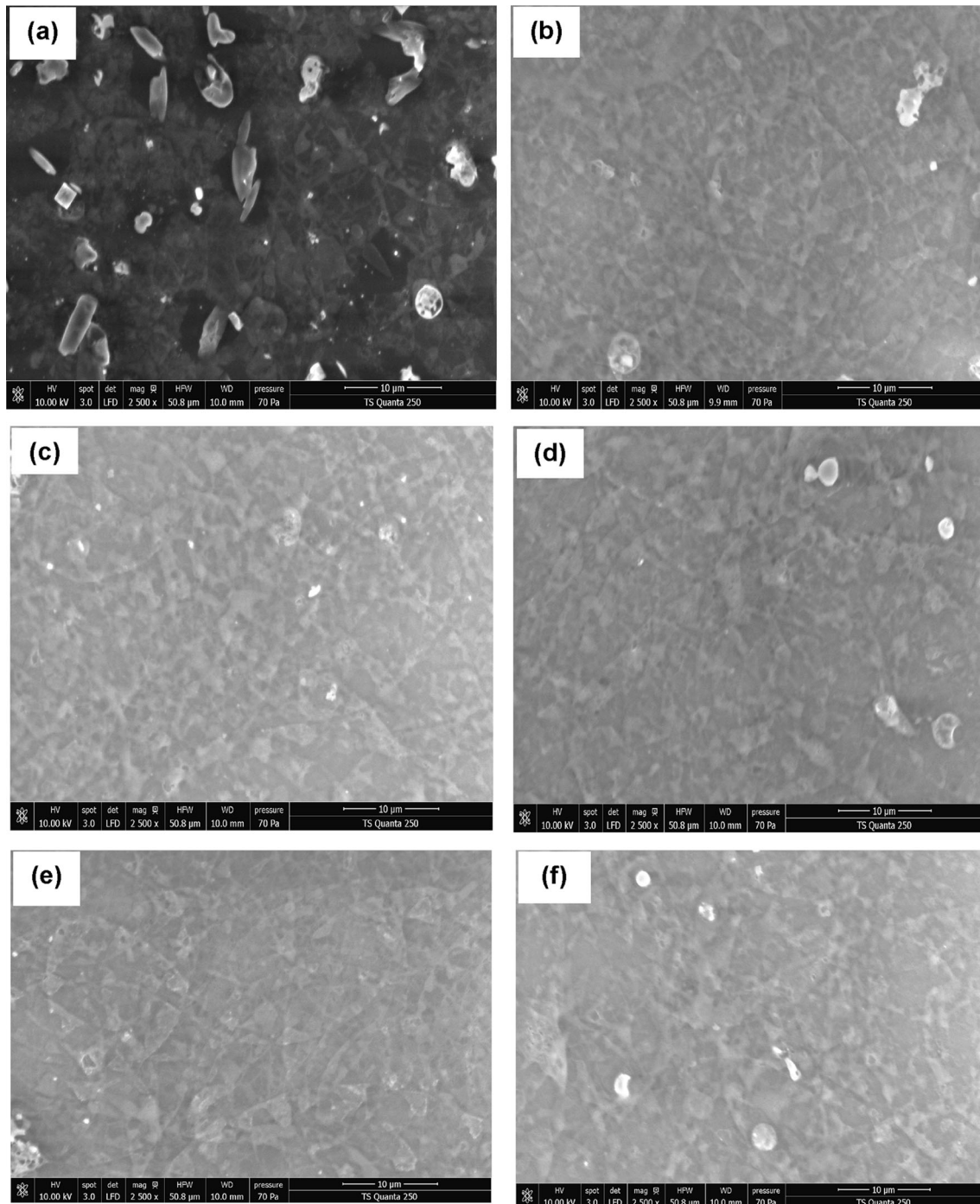
Fig. 2 SEM micrographs of samples: **a** pure La_2O_3, **b** La_2O_3:Ni(1%), **c** La_2O_3:Ni(2%), **d** La_2O_3:Ni(3%), **e** La_2O_3:Ni(4%) and **f** La_2O_3:Ni(5%)
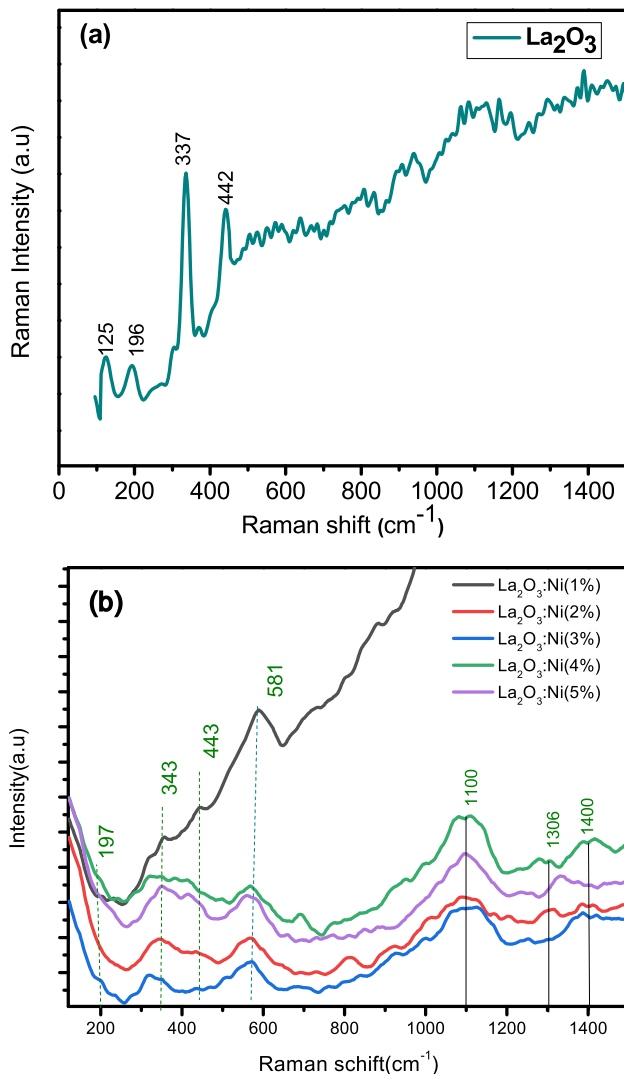
bands assigned at 125 cm^{-1} and 196 cm^{-1} are linked to cubic and hexagonal varieties, respectively [25]. This result is consistent with the XRD analysis. The intense peak appearing at 337 cm^{-1} corresponds to La–O vibration [26] while the band assigned at 442.52 cm^{-1} corresponds to Eg $_{v1}$ mode [27].

Figure 3b shows the Raman spectra of Ni doped La_2O_3 films with concentrations of 1 to 5%. It shows the existence of new bands located at 581 cm^{-1}, 1100 cm^{-1}, 1306 cm^{-1} and 1400 cm^{-1}. The two bands 1100 cm^{-1} and 1306 cm^{-1} could be related to NiO phase [28]. This can be related to the resulting

changes by Ni doping on the structural properties of La_2O_3 layers. The shift of the main band can be interpreted by a possible interaction between Ni and La_2O_3 material affecting La–O vibration.

3.2 Photoluminescence measurement (PL)

The study of prepared thin films by the photoluminescence PL technique can provide more details on the energy levels of different impurities and defects in undoped La_2O_3 and Ni doped La_2O_3 thin films. All PL measurements were recorded at 200 to 900 nm wavelength domain using 220 nm as excitation wavelength. Figure 4 shows that pure La_2O_3 and Ni doped La_2O_3 have similar shape of all PL curves.

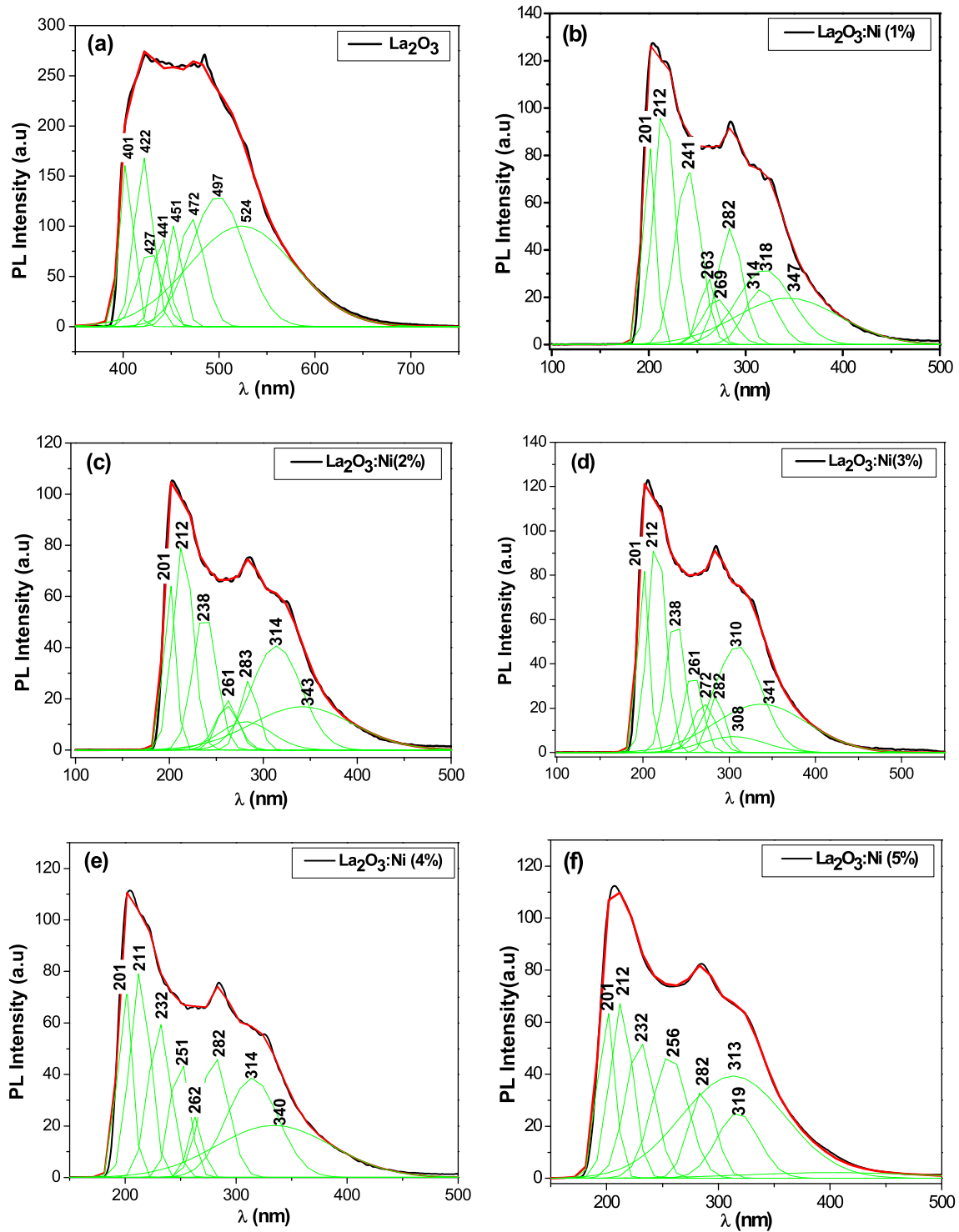Figure 5 shows the deconvolutions with Gaussian curves of undoped La_2O_3 and Ni doped La_2O_3 films. The emission interval of La_2O_3 is from 400 to 524 nm. The obtained emissions are related to inter-band transitions. The green emission is located at 524 nm which it is commonly related to oxygen vacancy [10]. The bleu emission at 461,472 and 487 nm may be linked to cation vacancy defects in La_2O_3. The violet emission at 401,422,427 and 441 nm is probably be interpreted by Stocks shift which is the origin of the certain defects [29]. It is noted that Ni doping leads to a shift in the emission interval that it becomes in the ultraviolet range. The quenching of the PL intensity of La_2O_3 when doped by nickel can be interpreted by the fact that Ni element decreases the charge carrier recombination. The same phenomenon is observed by Mrabet et al. when NiO is doped by La element [30]. This result is beneficial for possible sensitivity applications especially for photocatalytic applications [31, 32].

3.3 Complex impedance analysis

The electrical study was performed for undoped and Ni doped La_2O_3 using an impedance analyzer over a wide range of frequencies (1–1300 KHz) and temperature (623–803 k). The Nyquist diagrams obtained by plotting Z'' as function Z' are illustrated in Fig. 6. All the semicircles are described by a diameter and a maximum which decreases with increasing temperature. Indeed, this behavior can be interpreted by the decrease of the electrical resistivity of the elaborated layers [33]. This result can reflect a thermal activation

Fig. 3 Raman spectra of samples: a pure La_2O_3 and b La_2O_3: Ni (1–5%)
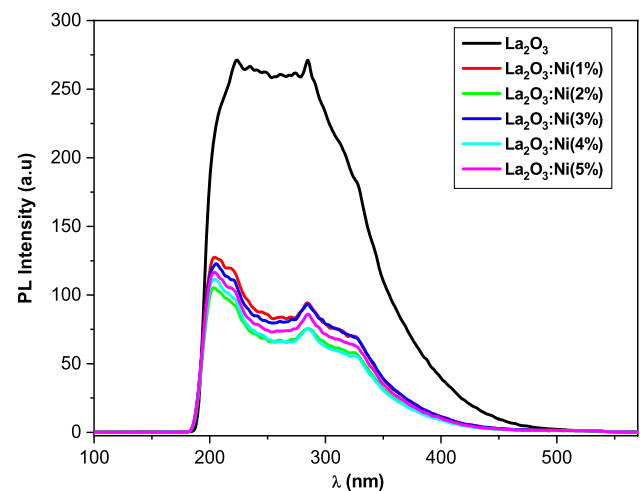
Fig. 4 PL spectra of pure La_2O_3 and La_2O_3: Ni (1–5%)

Fig. 5 Deconvolutions with Gaussian curves of samples: **a** La$_2$O$_3$: Ni, **b** La$_2$O$_3$: Ni (1%), **c** La$_2$O$_3$: Ni (2%), **d** La$_2$O$_3$: Ni (3%), **e** La$_2$O$_3$: Ni (4%) and **f** La$_2$O$_3$: Ni(5%)

of the electrical conductivity as well as a relaxation time distribution [34].

Figure 7 shows the angular frequencies dependence of Z'' at different temperatures. It is clearly seen that the maxima in Z'' peak shift towards higher frequency as a function of temperature. The reciprocal of the relaxation time $\omega_m = \frac{1}{\tau}$ is calculated from the

angular frequencies ω_m of the maximum peak [20]. The relaxation frequency is obtained from the Arrhenius law [35] given by:

$$\omega_m = \omega_0 e^{-\frac{E_a}{K_B T}} \qquad (1)$$

where, ω_0 is a constant. E_a and k_B are the activation energy and the Boltzmann constant, respectively.

The plot of the expression $Ln(f) = 1000/T$ (in inset of Fig. 7) proves the linearity of the function (Eq. 1) and it used to calculate E_a values.
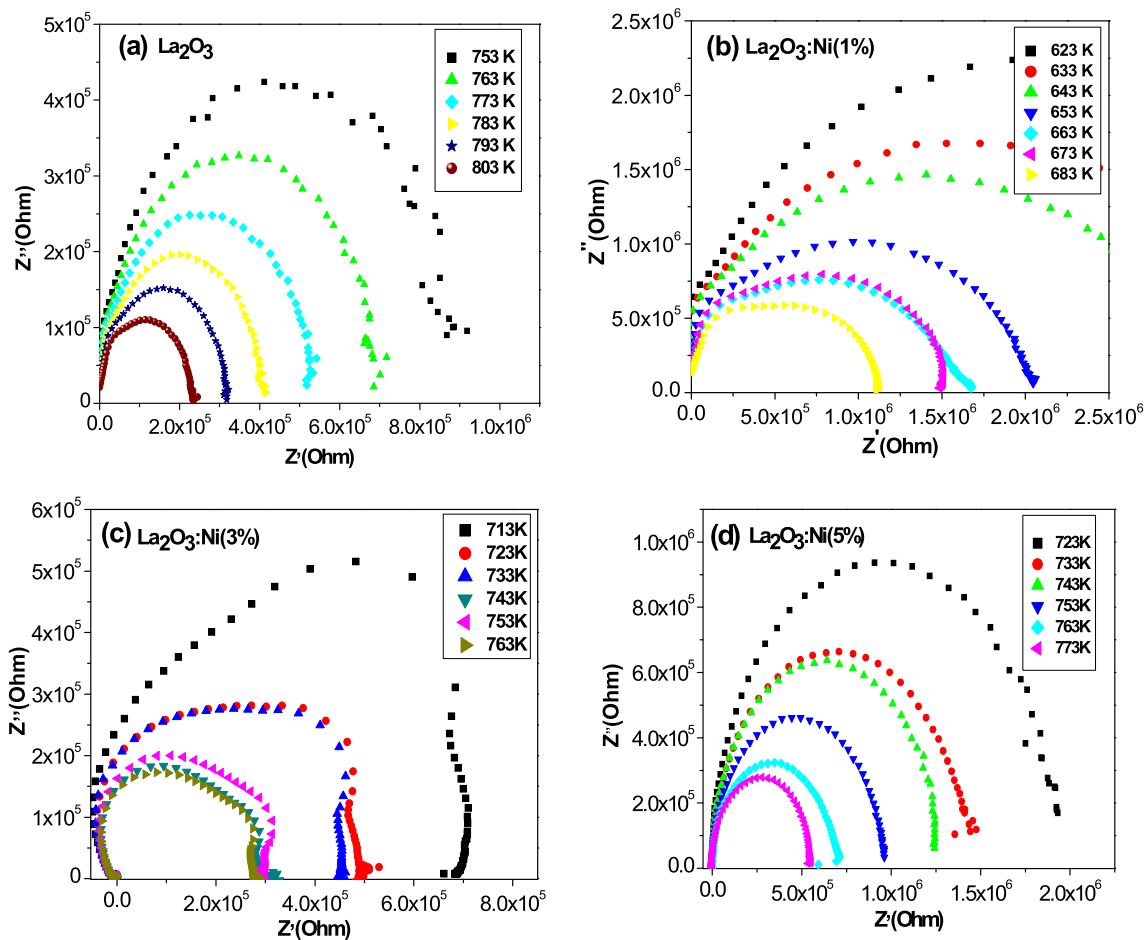
3.3.1 AC conductivity

The study of AC conductivity leads to a better understanding of the transport mechanism. Figure 8 shows the behavior of total conductivity *versus* frequency. The AC parameter can be examined by the the Jonscher's power law [20]:

$$\sigma_t = \sigma_{Dc} + \sigma_{Ac}(T, \omega) = A\omega^S \qquad (2)$$

The conductivity is DC type (denoted σ_{DC}) when the conductivity is low and independent of frequency. The value of "S" of all samples are less than 1, and it is frequency-dependent. The variation of the conductivity is weak at low frequencies. Contrariwise, the conductivity increases linearly at higher frequencies. We note that the frequency behavior is proportional to $A\omega^s$.

The temperature dependence of the exponent "S" allows to determinate the conduction process in such materials. Figure 9 shows the plot of "S" *versus* the temperature. It is found that "S" decreases with the increase of temperature. This behavior reveals that the conduction process is monitored by Elliott's CBH model [36].

Fig. 6 Complex impedance spectra of samples: **a** pure La_2O_3, **b** La_2O_3:Ni(1%), **c** La_2O_3:Ni(3%) and **d** La_2O_3: Ni(5%)
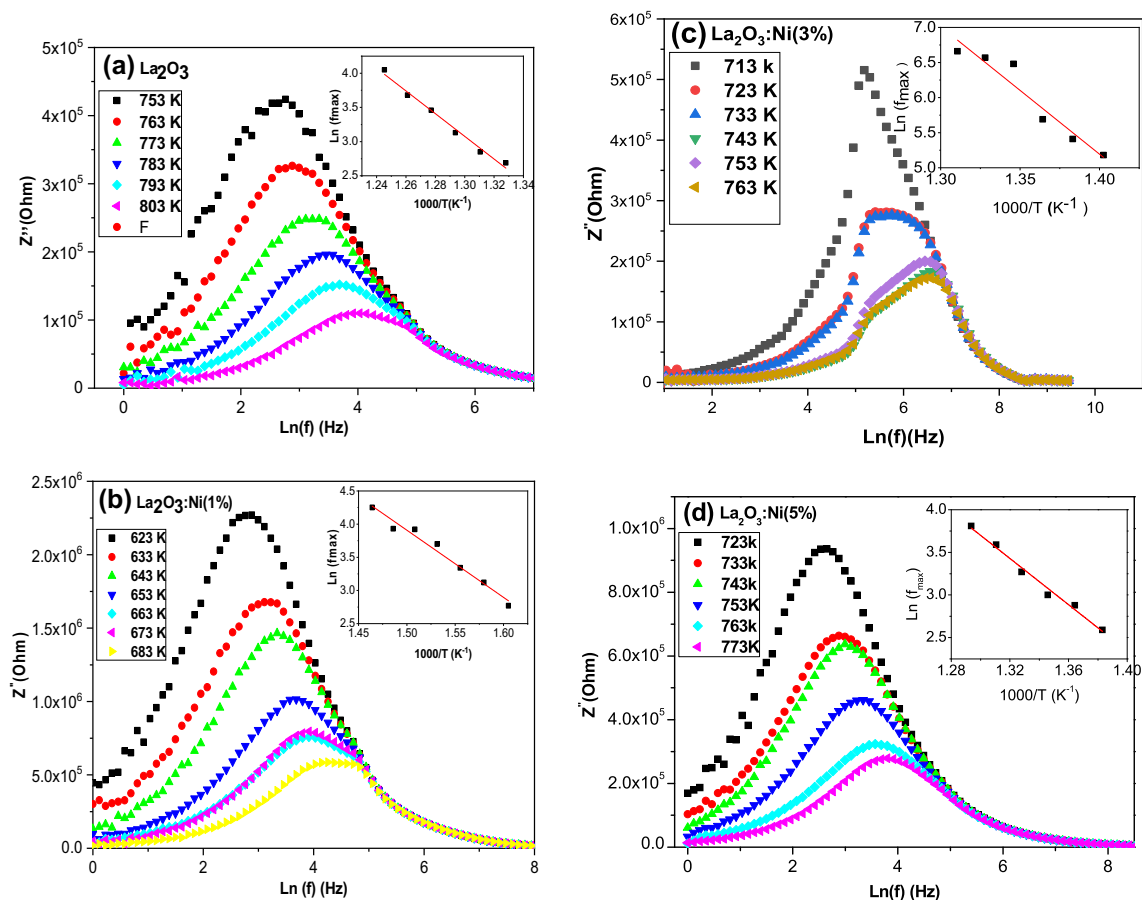
Fig. 7 Angular frequency dependence of Z'' at different temperature of samples: **a** pure La_2O_3, **b** La_2O_3:Ni(1%), **c** La_2O_3:Ni(3%) and **d** La_2O_3: Ni(5%)

3.3.2 DC conductivity

The DC conductivity measurement σ_{DC} plotted as a function of 1000/T in the insert of Fig. 8. The investigation of experimental data of the DC conductivity is performed via the Arrhenius law [37]:

$$\sigma_{Dc} = \frac{C}{T} e^{-\frac{E_{a(Dc)}}{k_B T}} \qquad (3)$$

where C, E_a and K_B are constants. It is observed that the DC conductivity of the different samples increases linearly with increasing temperature. The calculated values of E_a are listed in Table 1. These values are coherent with those calculated from the angular relaxation frequency (denoted hopping mechanism). By comparing the results obtained from the hopping mechanism with the DC conductivity, it is assumed that the conduction process is associated to a close transport mechanism (see Table 1).

3.4 Photocatalytic application

The tests of the photocatalytic activities of undoped and Ni doped La_2O_3 were carried out under sunlight. The degradation of the methylene blue (MB) was performed for various periods: 0, 60, 120, 180, 240 and 300 min. The degradation efficiency of this pollutant was determined by monitoring the characteristic peak of MB. Figure 10a shows the effect of photocatalytic degradation of MB for different Ni concentrations of 0–5% during 2H under sunlight. It can be seen that the presence of different layers leads to decrease the maximum characteristic absorption peak of the MB dye especially for La_2O_3: Ni 5%. It is noted that Ni doping improves the photocatalytic degradation efficiency. This is probably due to the fact that Ni makes changes in the band gap of La_2O_3 resulting the extension of the absorption solar energy spectrum. Likewise, Ni doping favors the presence of impurities like oxygen vacancies. It is assumed that
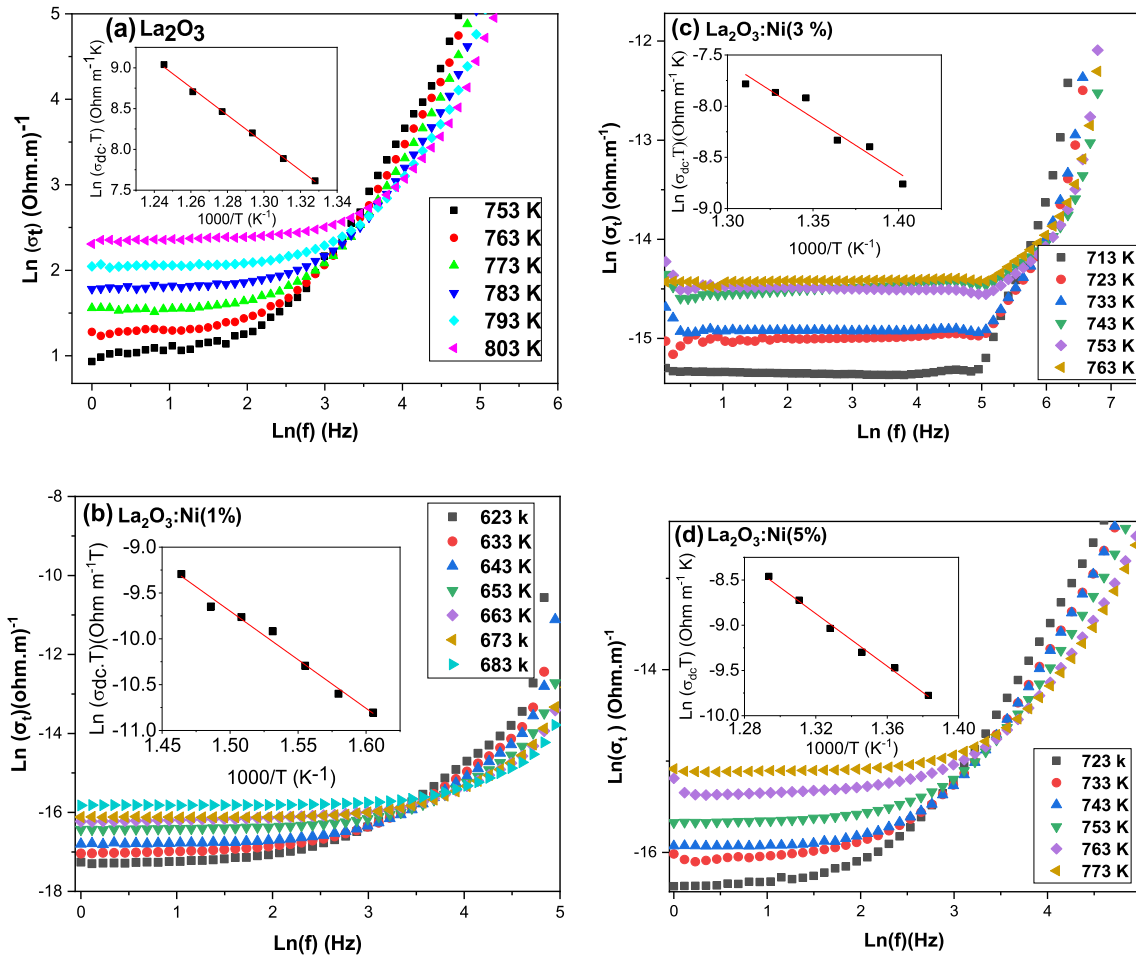
Fig. 8 Angular frequency dependence of total conductivity of samples: **a** pure La₂O₃, **b** La₂O₃:Ni(1%), **c** La₂O₃:Ni(3%) and **d** La₂O₃: Ni(5%)
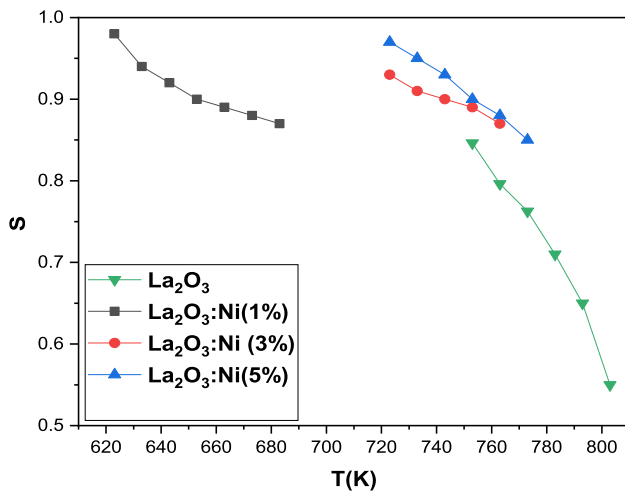
Fig. 9 Variation of exponent S *versus* T of samples: pure La₂O₃, La₂O₃:Ni(1%), La₂O₃:Ni(3%) and La₂O₃: Ni(5%)

Table 1 E_a activation energy and ω_m barrier weight of pure and Ni doped La₂O₃ thin films

	$E_a(Z'')$ (eV)	$E_a(Dc)$ (eV)	ω_m (eV)
Pure La₂O₃	1.41	1.46	1.72
La₂O₃:Ni (1%)	1.67	1.64	1.71
La₂O₃:Ni (3%)	1.73	1.76	1.81
La₂O₃:Ni (5%)	1.78	1.83	1.87

the photocatalytic property is influenced by many factors like: the morphology, the surface roughness, the porosity and also the degree of micro-structure of thin films [38]. Other investigation [39] reported that the photocatalytic performance can be affected by the charge transfer and the amount of oxygen vacancies. The present results show that Ni doping enhances the photocatalytic efficiency. This improvement is linked to the change of the surface roughness of the different
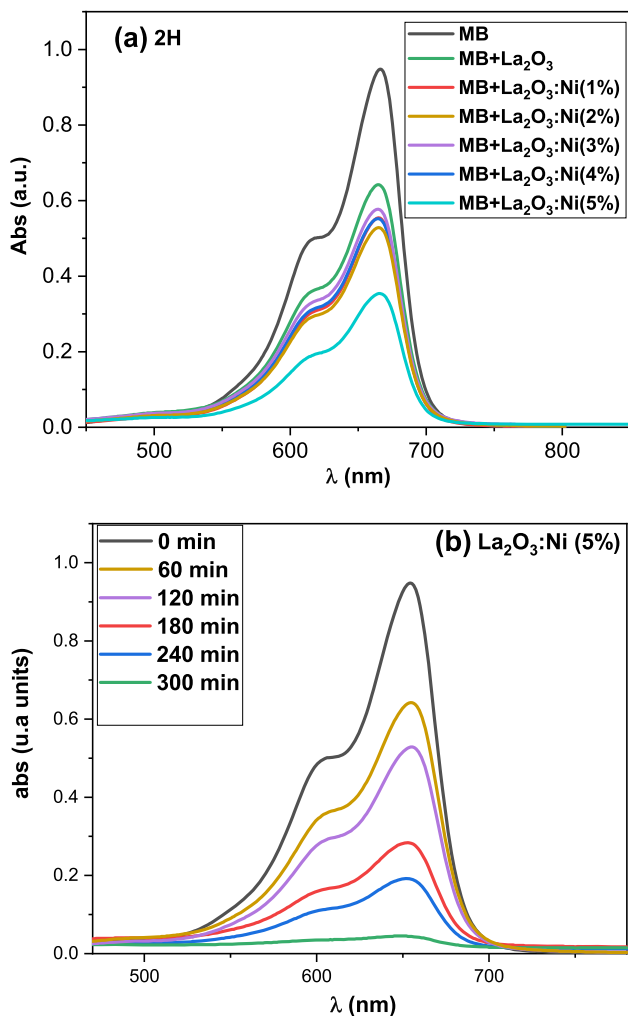
Fig. 10 Time-dependent absorption spectra of MB solution under sunlight irradiation in presence of: **a** pure La_2O_3 and La_2O_3: Ni (1–5%). **b** La_2O_3: Ni (5%) for different periods at 0 to 300 min

elaborated samples. As shown in Fig. 2, the morphology of Ni doped La_2O_3 thin films are better than the undoped one. Indeed, the diminution of the grain size improves the specific surface and thus enhances the photocatalytic efficiency. On the other hand, the rise of the amount of Nickel doping increases the amount of oxygen vacancies. This fact favors the existence of different defects states producing electron–hole pairs, especially for the high level for doping La_2O_3: Ni (5%).

For La_2O_3: Ni (5%), the curves of the absorption spectra of the MB solution as a function of time and under sunlight power (Fig. 10b) shows that after 300 min there is an almost total discoloration of the MB dye with disappearing of its maximum characteristic absorption.

The kinetic of different layers is determined from the plot of C_t/C_0 versus time exposition. The photocatalyst degradation kinetic is given by the following equation [40]:

$$\ln\left(\frac{C_t}{C_0}\right) = -kt \tag{4}$$

Figure 11 shows the plot of (C_t/C_0) versus time irradiation. The slope of the curve allows us to determinate K values (see Table 2). It is worth mentioning that La_2O_3:Ni (5%) sample exhibits the highest kinetic constant. This result confirms the photocatalytic performance of this doped film.

4 Conclusion

In summary, the elaboration of undoped La_2O_3 and Ni doped La_2O_3 was performed by means of the l spray pyrolysis. The structural and morphological properties of all samples were analyzed using different characterization techniques. The analysis by the XRD technique shows that the pure La_2O_3 crystallizes in a mixture phase, and it keeps the same structure after nickel doping. The SEM images show that the nickel improves the morphology surface of doped samples. Moreover, the electrical study reveals that the AC conductivity related to the law of the universal power and the quantization of charge carries can be achieved using the CBH model. Finally, Ni doping improves the photocatalytic efficiency, and
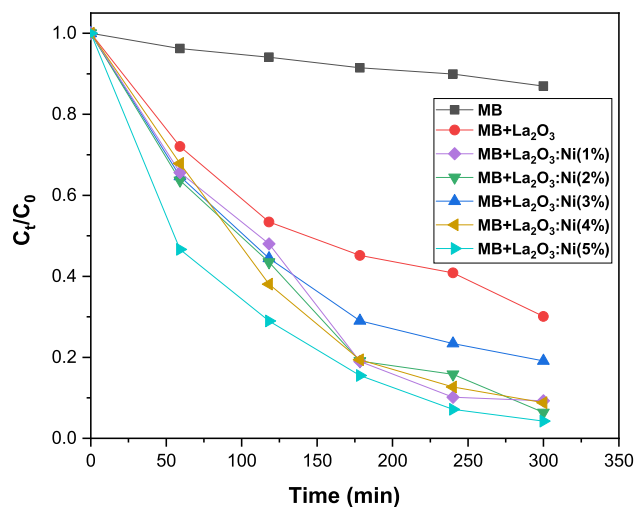
Fig. 11 Degradation rate of MB dye C_t/C_0 as a function of time exposition under sunlight for pure La_2O_3 and Ni doped La_2O_3 thin films

Table 2 Kinetic parameter of the methylene blue (MB), pure and Ni doped La_2O_3 thin films

Samples	Rate constant K (10^{-3} min^{-1})
MB	0.75
Pure La_2O_3	6.2
La_2O_3: Ni (1%)	13.5
La_2O_3: Ni (2%)	20.4
La_2O_3: Ni (3%)	9.2
La_2O_3: Ni (4%)	13.2
La_2O_3: Ni (5%)	22.6

the best activity is obtained for the sample La_2O_3: Ni (5%). This study seems interesting since large band gap energy oxide La_2O_3 can be used as photocatalytist under visible light with appropriate Ni content. Further works are planned to use such Ni doped thin films as gas and biosensors.

Acknowledgements

References

1. C. Michel, A. Martinez, CO sensing properties of novel nanostructured La_2O_3 microspheres. Sens. Actuator **208**, 355 (2015)

2. F.J. Jing, L. Wang, Y.W. Liu, K.Y. Fu, X.B. Zhao, R. Shen, Hemocompatibility of lanthanum oxide films fabricated by dual plasma deposition. Thin Solid Films **515**, 1219 (2006)

3. P. Nortier, M. Soustelle, Alumina carriers for automotive pollution control. Stud. Surf. Sci. Catal. **30**, 275 (1987)

4. M. Ghiasi, A. Malekzadeh, Characterization and photocatalytic properties of lanthanum oxy-carbonate, lanthanum oxide and lanthanum hydroxide nanoparticles. Superlattices Microstruct. **77**, 295 (2015)

5. J.B. Cheng, A.D. Lia, Q.Y. Shao, H.Q. Ling, D. Wua, Y. Wang, Y.J. Bao, M. Wang, Z.G. Liu, N.B. Ming, Growth and characteristics of La_2O_3 gate dielectric prepared by low pressure metalorganic chemical vapor deposition. Appl. Surf. Sci. **233**, 91 (2004)

6. K.B. Jinesh, V.A.T. Dam, J. Swerts, C. de Nooijer, S. van Elshocht, S.H. Brongersma, M. Crego-Calama, Room-temperature CO_2 sensing using metal–insulator–semiconductor capacitors comprising atomic-layer-deposited La_2O_3 thin films. Sens. Actuators B Chem. **156**, 276 (2011)

7. X.F. Ding, Y.J. Liu, L. Gao, L.C. Guo, Effects of cation substitution on thermal expansion and electrical properties of lanthanum chromites. J. Alloy. Compds. **425**, 318 (2006)

8. A. Weidenkaff, R. Robert, M. Aguirre, L. Bocher, T. Lippert, S. Canulescu, Development of thermoelectric oxides for renewable energy conversion technologies. Renew. Energy **33**, 342 (2008)

9. R. Jbeli, A. Boukhachem, F. Saadallah, S. Alleg, M. Amlouk, H. Ezzaouïa, Synthesis and physical properties of Fe doped La_2O_3 thin films grown by spray pyrolysis for photocatalytic applications. Mater. Res. Expres. **6**, 066414 (2019)

10. R. Jbeli, A. Boukhachem, I. Ben Jemaa, N. Mahdhi, F. Saadallah, H. Elhouichet, S. Alleg, M. Amlouk, H. Ezzaouïa, An enhancement of photoluminescence property of Ag doped La_2O_3 thin films at room temperature. Spectrochim. Acta Part A Mol Biomol. Spectrosc. **184**, 71 (2017)

11. C. Bilel, R. Jbeli, I. Ben Jemaa, A. Boukhachem, F. Saadallah, M. Amlouk, H. Ezzaouïa, Physical investigations on Copper doped La_2O_3 thin films for photocatalytic application. J. Mater. Sci. Mater. Electron. **31**, 7398 (2020)

12. R. Gunawidjaja, H. Diez-y-Riega, H. Eilers, Synthesis and characterizations of spherical Eu:La_2O_3 and relatedcore/shell nanoparticles. Powder Technol. **271**, 255 (2015)

13. S. Li, Y. Lin, Y. Wu, Y. Wu, X. Li, W. Tian, Ni doping significantly improves dielectric properties of La_2O_3 films. J. Alloys Compd. **822**, 153469 (2020)

14. F. Nolting, A. Scholl, J. Stöhr, J.W. Seo, J. Fompeyrine, H. Siegwart, J.-P. Locquet, S. Anders, J. Lüning, E.E. Fullerton, M.F. Toney, M.R. Scheinfein, H.A. Padmore, Direct observation of the alignment of ferromagnetic spins by antiferromagnetic spins. Nature **405**, 767 (2000)

15. C. Yang, H. Fan, S. Qiu, Y. Xi, Y. Fu, Microstructure and dielectric properties of La_2O_3 films prepared by ion beam assistant electron-beam evaporation. J. Non-Cryst. Solids **355**, 33 (2009)

16. M.F. Vignolo, S. Duhalde, M. Bormioli, G. Quintana, M. Cervera, J. Tocho, Structural and electrical properties of lanthanum oxide thin films deposited by laser ablation. Appl. Surf. Sci. **198**, 522 (2002)

17. A.A. Dakhel, Structural and ac electrical properties of oxidized La and La-Mn thin films grown on Si substrates. Mater. Chem. Phys. **102**, 266 (2007)

18. N.K. Park, D.K. Kang, B.H. Kim, S.J. Jo, J.S. Ha, Effects of growth temperature and oxidant feeding time on residual C-and N-related impurities and Si diffusion behavior in atomic layer-deposited La_2O_3 thin films. Appl. Surf. Sci. **252**, 8506 (2006)

19. W. Zhang, W. Liu, C. Wang, Characterization and tribological investigation of SiO$_2$ and La$_2$O$_3$ sol–gel films. Appl. Surf. Sci. **185**, 34 (2001)

20. S.S. Kale, K.R. Jadhav, P.S. Patil, T.P. Gujar, C.D. Lokhande, Characterizations of spray-deposited lanthanum oxide (La$_2$O$_3$) thin films. Mater. Lett. **59**, 3007 (2005)

21. A. Boukhachem, B. Ouni, M. Karyaoui, A. Madani, R. Chtourou, M. Amlouk, Structural, opto-thermal and electrical properties of ZnO: Mo sprayed thin films. Mater. Sci. Semicond. Process. **15**, 282 (2012)

22. A. Boukhachem, C. Bouzidi, R. Boughalmi, R. Ouerteni, M. Kahlaoui, B. Ouni, H. Elhouichet, M. Amlouk, Physical investigations on MoO$_3$ sprayed thin film for selective sensitivity applications. Ceram. Intern. **40**, 13427 (2014)

23. M. Uzunova, M. Kostadinov, J. Georgieva, C. Dushkin, D. Todorovsky, N. Philippidis, I. Poulios, S. Sotiropoulos, Photoelectrochemical characterisation and photocatalytic activity of composite La$_2$O$_3$–TiO$_2$ coatings on stainless steel. Appl. Catal. B Environ. **73**, 23 (2007)

24. A.S. Weber, A.M. Grady, R.T. Koodali, Lanthanide modified semiconductor photocatalysts. Catal. Sci. Technol. **4**, 683 (2012)

25. A. Orera, G. Larraz, M.L. Sanjuán, Spectroscopic study of the competition between dehydration and carbonation effects in La$_2$O$_3$-based materials. J. Eur. Ceram. Soc. **33**, 2103 (2013)

26. J. Cui, G.A. Hope, Raman and fluorescence spectroscopy of CeO$_2$, Er$_2$O$_3$, Nd$_2$O$_3$, Tm$_2$O$_3$, Yb$_2$O$_3$, La$_2$O$_3$, and Tb$_4$O$_7$. J. Spectrosc. **2015**, 8 (2015)

27. J.H. Denning, S.D. Ross, The vibrational spectra and structures of rare earth oxides in the A modification. J. Phys. C: Solid State Phys. **5**, 1123 (1972)

28. A. Loukil, A. Boukhachem, M. Ben Amor, M. Ghamnia, K. Raouadi, Effects of potassium incorporation on the structural, optical, vibrational and electrical properties of NiO sprayed thin films for p-type optical windows. Ceram. Int. **42**, 8274 (2016)

29. S. Mochizuki, T. Saito, Intrinsic and defect-related luminescence of NiO. Phys. B **404**, 4850 (2009)

30. C. Mrabet, M. Ben Amor, A. Boukhachem, M. Amlouk, T. Manoubi, Physical properties of La-doped NiO sprayed thin films for optoelectronic and sensor applications. Ceram. Int. **42**, 5963 (2016)

31. J.G. Yu, H.G. Yu, B. Chen, X.J. Zhao, J.C. Yu, W.K. Ho, The effect of calcination temperature on the surface microstructure and photocatalytic activity of TiO$_2$ thin films prepared by liquid phase deposition. J. Phys. Chem. B **107**, 13871 (2003)

32. M.M. El-Nahass, H.A.M. Ali, M. Saadeldin, M. Zaghllol, AC conductivity and dielectric properties of bulk tungsten trioxide (WO$_3$). Phys. B **407**, 4453 (2012)

33. T. Nagata, T. Shimura, A. Ashida, N. Fujimura, T. Ito, Electro-optic property of ZnO: X (X=Li, Mg) thin films. J. Cryst. Growth **237**, 533 (2002)

34. A.E. Bekheet, N.A. Hegab, Ac conductivity and dielectric properties of Ge20Se75In5 films. Vacuum **83**, 391 (2000)

35. A.K. Jonscher, The universal dielectric response. Nature **267**, 673 (1977)

36. B. Ouni, M. Haj Lakhdar, R. Boughalmi, T. Larbi, A. Boukhachem, A. Madani, K. Boubaker, M. Amlouk, Investigation of electrical and dielectric properties of antimony oxide (Sb$_2$O$_4$) semiconductor thin films for TCO and optoelectronic applications. J. Non-Cryst. Solids **367**, 1 (2013)

37. A. Arfaoui, A. Mhamdi, B. Khalfallah, S. Belgacem, M. Amlouk, Physical characterizations of the sprayed ZrMo$_2$O$_8$ thin flms. Appl. Phys. A **125**, 517 (2019)

38. T. Larbi, M.A. Amara, B. Ouni, M. Amlouk, Enhanced photocatalytic degradation of methylene blue dye under UV-sunlight irradiation by cesium doped chromium oxide thin films. Mater. Res. Bull. **95**, 152 (2017)

39. G. Kenanakis, N. Katsarakis, Ultrasonic spray pyrolysis growth of ZnO and ZnO: Al nanostructured films: application to photocatalysis. Mater. Res. Bull. **60**, 752 (2014)

40. P. Jongnavakit, P. Amornpitoksuk, S. Suwanboon, N. Ndiege, Preparation and photocatalytic activity of Cu-doped ZnO thin films prepared by the sol–gel method. Appl. Surf. Sci. **258**, 8192 (2012)